KeAi

CHINESE ROOTS
GLOBAL IMPACT

Contents lists available at ScienceDirect

Petroleum Science

journal homepage: www.keaipublishing.com/en/journals/petroleum-science



Original Paper

Direct inversion of 3D seismic reservoir parameters based on dual learning networks



Yang Zhang, Hao Yang*

Research Institute of Petroleum Exploration & Development, Petrochina, Beijing, 100083, China

ARTICLE INFO

Article history: Received 8 December 2024 Received in revised form 26 February 2025 Accepted 29 May 2025 Available online 30 May 2025

Edited by Meng-Jiao Zhou

Keywords:
Seismic inversion
Rock physics
Deep learning
Tight sand
Reservoir predict

ABSTRACT

Tight sandstone has become an important area in gas exploration. In this study, we propose a 3D seismic reservoir parameter inversion method for tight gas-bearing sandstone reservoirs using dual neural networks. The first network referred to as the inversion network, receives seismic data and predicts reservoir parameters. At well locations, these predictions will be validated based on actual reservoir parameters to evaluate errors. For non-well locations, synthetic seismic data are generated by the application of rock physics forward modeling and seismic reflection coefficient equations. The errors are then calculated by comparing synthetic seismic data with actual seismic data. During the rock physics forward modeling, pseudo reservoir parameters are derived by perturbing the actual reservoir parameters, which are then used to generate pseudo elastic parameters through the modeling. Both the actual and pseudo parameters are then used to train the second network, referred to as the rock physics network. By incorporating the rock physics network, the method effectively alleviates issues such as gradient explosion that may arise from directly integrating rock physics computations into the network, while the inclusion of pseudo parameters enhances the network's generalization capability. The proposed method enables the direct inversion of porosity, clay content, and water saturation from pre-stack seismic data using deep learning, thereby achieving quantitative predictions of reservoir rock physical parameters. The application to the field data from tight sandstone gas reservoirs in southwestern China demonstrates the method has the good capability of indicating the gas-bearing areas and provide high resolution.

© 2025 The Authors. Publishing services by Elsevier B.V. on behalf of KeAi Communications Co. Ltd. This is an open access article under the CC BY-NC-ND license (http://creativecommons.org/licenses/by-nc-nd/4.0/).

1. Introduction

Changes in reservoir parameters influence elastic properties, including P-wave velocity, S-wave velocity, and density, thereby affecting seismic responses (Chiappa and Mazzotti, 2009; Luo et al., 2019; Zhao et al., 2014). Reservoir parameter prediction is a crucial step in characterizing oil and gas reservoirs, as it serves as a fundamental basis for reservoir evaluation, influencing well selection and development strategies (Grana et al., 2022). Seismic data can be used to predict reservoir parameters, with pre-stack seismic inversion and rock physics models playing critical roles.

E-mail address: yanghao01@petrochina.com.cn (H. Yang).

Peer review under the responsibility of China University of Petroleum (Beijing).

Reservoir parameter prediction can be categorized into indirect and direct methods based on the number of inversion steps, both of which seek to create correlations between seismic data and reservoir characteristics (Bosch et al., 2010). Indirect inversion mainly involves two steps: seismic data are first inverted to obtain elastic parameters, which are then used to predict reservoir parameters (Ba et al., 2017; Grana, 2016). Inversion processes are frequently ill-posed due to constraints like noise and bandwidth, which calls for the use of Bayesian theory for the assessment of uncertainty (Buland and Omre, 2003; Junhwan et al., 2022; Wang et al., 2022a). Some also use grid search or rock physics templates for parameter prediction (Jiang and Spikes, 2016; Luo et al., 2019). Direct inversion, on the other hand, enables the direct inversion of intricate, nonlinear relationships between seismic data and reservoir properties by incorporating reservoir parameters into seismic reflection equations (Aleardi et al., 2017; Guo et al., 2022; Li et al., 2020; Pan et al., 2017; Pan and Zhang, 2019). Compared to the indirect inversion methods, the direct inversion methods

^{*} Corresponding author.

merge two steps into one, potentially reducing errors in the inversion process.

Rock physics models serve as a bridge between reservoir parameters and elastic parameters. Building a robust rock physics model is a critical part of the inversion process whether direct or indirect inversion methods are being used. Rock physics models can be broadly categorized into statistical and theoretical models based on the construction approach. Statistical rock physics models use statistical methods to establish the relationship between reservoir parameters and elastic properties (Bachrach, 2006; Grana and Rossa, 2010). These models are relatively simple to construct and do not require rigorous physical derivations, but their applicability is often limited to specific regions. On the other hand, theoretical rock physics models are based on rock physics theories and are more accurate and widely applicable (Gassmann, 1951; Hill, 1952; Kuster and Toksöz, 1974; Reuss, 1929; Voigt, 1966; Wood, 1955; Xu and White, 1995). However, they are more complex to calculate and present greater challenges during inversion.

The above methods are mostly grounded in Bayesian theory and concentrate on 2D reservoir parameter inversion. Innovative techniques in disciplines like computer vision have emerged in deep learning, which has witnessed rapid progress in recent years (Diakogiannis et al., 2020; Goodfellow et al., 2020; He et al., 2015, 2016; Huang et al., 2018; Long et al., 2015; Ronneberger et al., 2015; Simonyan and Zisserman, 2015). The relationship between reservoir parameters and seismic data in tight sandstone, meanwhile, is highly nonlinear. Deep learning excels in fitting such complex relationships, leading to its increasing application in geophysical inversion (Alfarraj and AlRegib, 2019; Biswas et al., 2019; Das et al., 2018; Das and Mukerji, 2020; Leite and Vidal, 2011; Sang et al., 2021; Sun et al., 2024a; Sun et al., 2023, 2024b; Wang et al., 2022b, 2024; Zhang et al., 2022a; Zhang et al., 2022a,b; Zhao et al., 2023; Zheng et al., 2023; Zhu et al., 2022).

Building upon this background, we propose an intelligent method for directly inverting reservoir parameters from 3D prestack seismic data. The method generates pseudo elastic parameters by using the approximate Xu-White model and pseudo reservoir parameters that are derived by perturbing actual reservoir parameters. The rock physics network (RP-Net) is trained using pseudo parameters and actual parameters. During rock physics modeling, this study considers variable aspect ratios instead of fixed ones, which more accurately represent the true pore structure of rocks. Equipped with the approximation Zoeppritz equation (Aki and Richards, 2009) and RP-Net, a forward

operator between reservoir parameters and seismic data can be constructed to enable reservoir parameter inversion. In this study, we used the method of trace-by-trace inversion. After merging the inline and xline of the 3D seismic data volume, we obtain multiple 1D time-domain seismic data. Then, after inputting the seismic data into the Inv-Net, the output reservoir data is reorganized into 3D data. To better evaluate the effectiveness and improvements of the proposed method, we introduce the method of directly embedding the theoretical rock physics model (RP-Model) into the inversion network (Inv-Net) for comparison. The proposed method is called "RP-Net + Inv-Net", and the method used for comparison is called "RP-Model + Inv-Net". The overall framework of this study is as follows: initially, the steps involved in rock physics modeling are introduced, with a brief analysis of the impact of some reservoir parameters on rock elastic properties. The construction of RP-Net and Inv-Net is then explained, and the suggested method's efficacy is confirmed by applying it to a realworld field case. A discussion of the results and conclusion are finally made.

2. Method

2.1. RP-model

The Xu-White model is a rock physics model used to predict the elastic properties of sand-shale mixtures. The model assumes that the primary mineral components of the mixture are clay and quartz, divides the pore space into shale pores and sandstone pores, and considers the pore fluids as a mixture of brine and gas. Four steps make up the calculation process: estimating the equivalent elastic moduli of the rock matrix, estimating the equivalent modulus of the saturated fluid, and using fluid substitution to estimate the final equivalent modulus of the saturated rock. We use the Xu-White model for rock physics modeling, and the specific modeling process is illustrated in Fig. 1.

First, the equivalent modulus of the rock matrix is estimated. For rocks with relatively homogeneous composition, the Voigt-Reuss-Hill averaging method can be used to calculate the equivalent modulus of the rock matrix. We follow this approach in this paper, as shown by

$$M_{\rm V} = f_{\rm clay} M_{\rm clay} + f_{\rm quartz} M_{\rm quartz}$$
 (1)

$$1 / M_{R} = f_{\text{clay}} / M_{\text{clay}} + f_{\text{quartz}} / M_{\text{quartz}}$$
 (2)

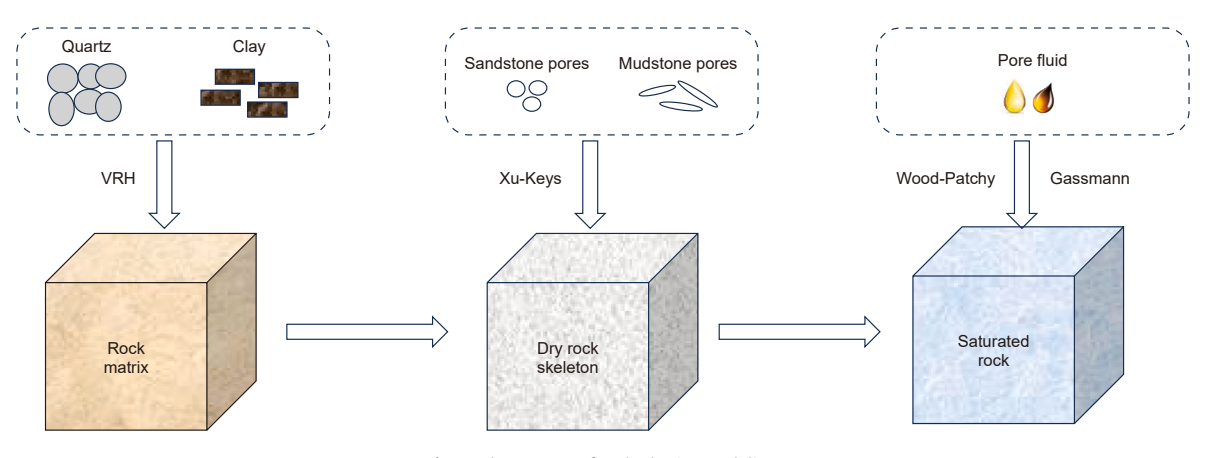


Fig. 1. The process of rock physics modeling.

$$M_{VRH} = (M_V + M_R) / 2$$
 (3)

where $f_{\rm clay}$ and $M_{\rm clay}$ represent the volume fraction and elastic modulus of clay, respectively, and $f_{\rm quartz}$ and $M_{\rm quartz}$ represent the volume fraction and elastic modulus of quartz, respectively. $M_{\rm V}$ represents the elastic modulus of the rock matrix calculated using the Voigt average, $M_{\rm R}$ represents the elastic modulus calculated using the Reuss average, and $M_{\rm VRH}$ represents the elastic modulus of the rock matrix calculated using the Voigt-Reuss-Hill average.

After obtaining the elastic modulus of the rock matrix, the dry rock approximate equation (Keys and Xu, 2002) is used to calculate the elastic modulus of the dry rock frame. Assuming the elastic modulus of the inclusion is 0, the specific equations can be expressed as

$$p = \frac{1}{3} \sum_{l=S,C} \nu_l T_{iijj}(\alpha_l) \tag{4}$$

$$q = \frac{1}{5} \sum_{l=S,C} \nu_l F(\alpha_l) \tag{5}$$

$$K_{\text{drv}}(\phi) = K_0 (1 - \phi)^p$$
 (6)

$$\mu_{\rm drv}(\phi) = \mu_0 (1 - \phi)^q \tag{7}$$

where p and q are a set of coefficients related to the sandstone and mudstone pores (Berryman, 1980), with the detailed calculation process provided in Appendix A. K_0 and μ_0 represent the bulk modulus and shear modulus of the rock matrix. $K_{\rm dry}(\phi)$ and $\mu_{\rm dry}(\phi)$ is the dry rock bulk modulus and shear modulus for porosity ϕ .

Next, the Wood-Patchy equation is used to calculate the elastic modulus of the mixed fluid, and the specific equations can be expressed as

$$K_{\rm f}^{\rm W} = 1 / (S_{\rm W} / K_{\rm W} + (1 - S_{\rm W}) / K_{\rm g})$$
 (8)

$$K_{\rm f}^{\rm p} = S_{\rm w} K_{\rm w} + (1 - S_{\rm w}) K_{\rm g}$$
 (9)

$$K_{\rm f} = \left(K_{\rm f}^{\rm p} + K_{\rm f}^{\rm w}\right) / 2 \tag{10}$$

where $S_{\rm w}$ represents the water saturation, $K_{\rm w}$ and $K_{\rm g}$ represent the bulk modulus of water and gas, respectively, and $K_{\rm f}^{\rm w}$ and $K_{\rm f}^{\rm p}$ represent the bulk modulus of the mixed fluid calculated using the Wood equation and the Patchy model, respectively. $K_{\rm f}$ represents the final calculated bulk modulus of the mixed fluid.

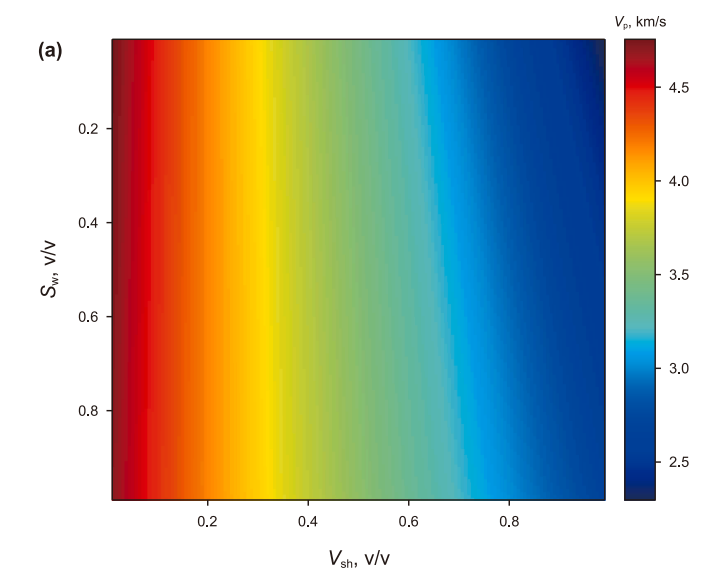
Then, fluid substitution is performed using the Gassmann equation to obtain the elastic modulus of the saturated rock, with the specific equations can be expressed as

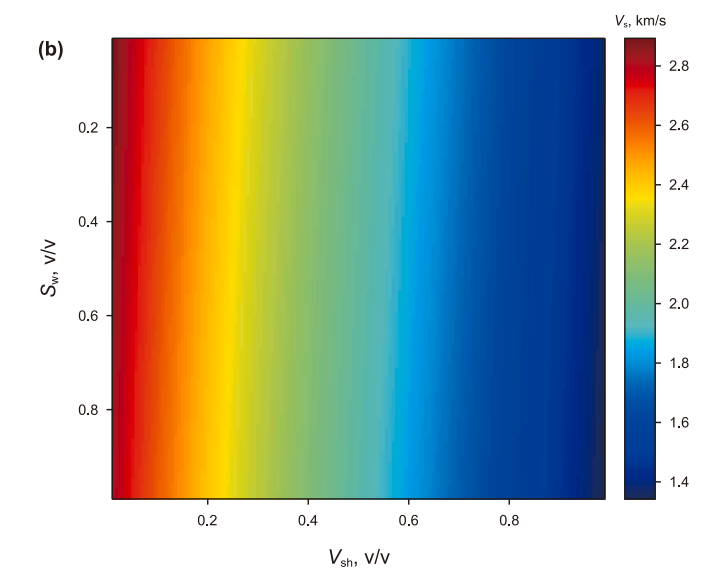
$$K_{\text{sat}} = K_{\text{dry}} + \frac{\left(1 - K_{\text{dry}} / K_{\text{m}}\right)^{2}}{\phi / K_{\text{f}} + (1 - \phi) / K_{\text{m}} + K_{\text{dry}} / K_{\text{m}}^{2}}$$
 (11)

$$\mu_{\text{sat}} = \mu_{\text{dry}} \tag{12}$$

where ϕ represents the total porosity, which is the sum of sandstone and mudstone porosity. K_{sat} and μ_{sat} represent the bulk modulus and shear modulus of the saturated rock, respectively.

Finally, the P-wave and S-wave velocities and density of the saturated rock are calculated using the following equations:





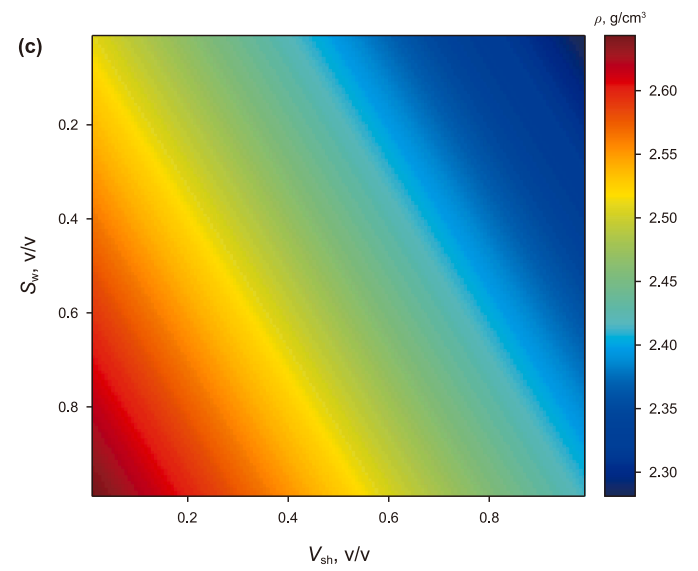


Fig. 2. The influence of S_W and V_{sh} on elastic parameters. (a) The impact of S_W and V_{sh} on V_D . (b) The impact of S_W and V_{sh} on V_S . (c) The impact of S_W and V_{sh} on ρ .

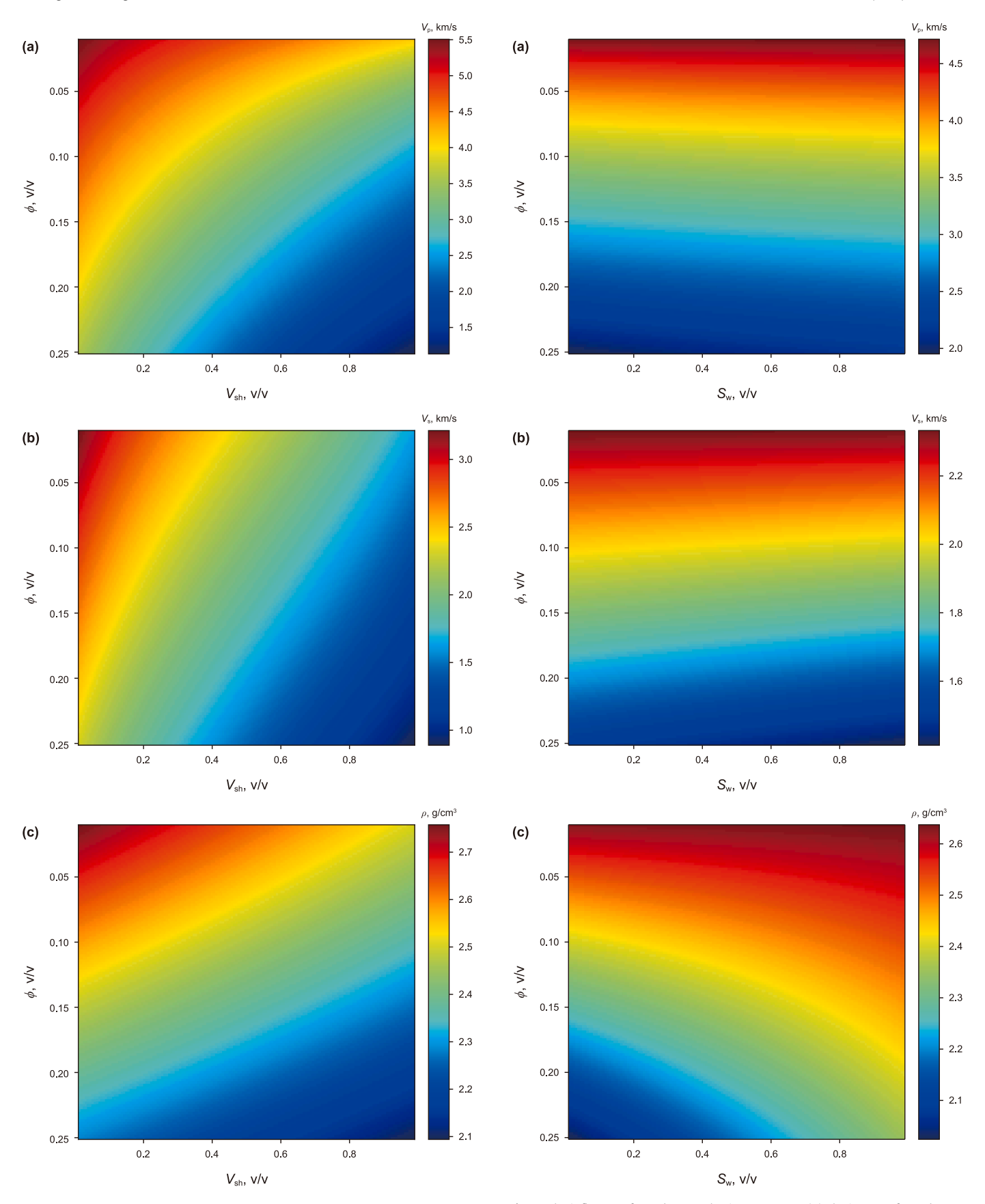


Fig. 3. The influence of ϕ and $V_{\rm sh}$ on elastic parameters. (a) The impact of ϕ and $V_{\rm sh}$ on $V_{\rm p}$. (b) The impact of ϕ and $V_{\rm sh}$ on $V_{\rm s}$. (c) The impact of ϕ and $V_{\rm sh}$ on ρ .

Fig. 4. The influence of ϕ and $S_{\rm W}$ on elastic parameters. **(a)** The impact of ϕ and $S_{\rm W}$ on $V_{\rm p}$. **(b)** The impact of ϕ and $S_{\rm W}$ on $V_{\rm s}$. **(c)** The impact of ϕ and $S_{\rm W}$ on ρ .

$$\rho_{\rm m} = f_{\rm clav} \, \rho_{\rm clav} + f_{\rm quartz} \, \rho_{\rm quartz} \tag{13}$$

$$\rho_{\mathbf{f}} = S_{\mathbf{W}} \rho_{\mathbf{W}} + (1 - S_{\mathbf{W}}) \rho_{\mathbf{g}} \tag{14}$$

$$\rho = \phi \rho_{\rm f} + (1 - \phi) \rho_{\rm m} \tag{15}$$

$$V_{\rm P} = \sqrt{\left(K_{\rm sat} + \frac{4}{3}\mu_{\rm sat}\right)/\rho} \tag{16}$$

$$V_{\rm S} = \sqrt{\mu_{\rm sat} / \rho} \tag{17}$$

where $\rho_{\rm clay}$ and $\rho_{\rm quartz}$ represent the density of clay and quartz, $\rho_{\rm w}$ and $\rho_{\rm g}$ represent the density of formation water and gas, and $\rho_{\rm m}$, $\rho_{\rm f}$, and ρ represent the density of the rock matrix, the mixed fluid, and the saturated rock, respectively. $V_{\rm P}$ and $V_{\rm S}$ represent the P-wave and S-wave velocities of the saturated rock.

Combining Eqs. (1)–(17), we can derive the corresponding elastic parameters from the reservoir parameters, as shown in the following equation:

$$E_{\text{Model}}\left(V_{p}, V_{s}, \rho\right) = \text{Model}^{\text{RP}}(\phi, S_{w}, V_{\text{sh}}, P)$$
(18)

where P denotes other parameters required for rock physics modeling, such as elastic modulus, pore aspect ratio, density, etc. $\mathsf{Model}^\mathsf{RP}(\cdot)$ denotes the RP-Model, and $E_{\mathsf{Model}}(\cdot)$ represents the elastic parameters derived through the RP-Model.

2.2. Effects of reservoir parameters

The pore aspect ratio of rocks, for example, is one reservoir property that significantly affects elastic properties. In general, the aspect ratio of the sand-related pores (α_s) typically has a bigger value than that of the clay-related pores (α_c) , with the latter having a greater impact on the elastic properties of the rock, especially in sandstones that contain clay minerals (Sams and Andrea, 2001; Smith and Gidlow, 1987). In most cases, the pore aspect ratio cannot be directly measured. In this study, suitable pore aspect ratios were optimized during the modeling process by minimizing the difference between the predicted and actual P-wave and S-wave velocities, as shown in the following equation:

$$\left(\ddot{\alpha}_{S}, \ddot{\alpha}_{C}\right) = \operatorname{argmin} \left\| V_{P_{-}S}^{\text{pred}}(\phi, V_{\text{sh}}, S_{\text{w}}, \alpha_{S}, \alpha_{C}) - V_{P_{-}S}^{\log} \right\|_{2}$$
(19)

where $V_{P,S}^{log}$ and $V_{P,S}^{pred}$ represent the P-wave and S-wave velocities from well data and rock physics modeling, respectively, while $\ddot{\alpha}_{S}$ and $\ddot{\alpha}_{C}$ represent the optimized aspect ratios of sandstone and mudstone pores. Additionally, some studies have experimentally obtained the following statistical relationship between α_{S} , ϕ and V_{sh} (Sams and Andrea, 2001):

$$\alpha_{\rm S} = 0.17114 - 0.24477 \cdot \phi + 0.004314 \cdot V_{\rm sh} \tag{20}$$

During the rock physics modeling, we use initial α_s obtained by Eq. (20) and a given initial α_c to optimize the most suitable α_s and α_c .

Next, we used the established rock physics model for forward modeling analysis to illustrate the effects of changes in ϕ , $V_{\rm sh}$, $S_{\rm w}$, and pore aspect ratio on the elastic properties. The results are shown in Figs. 2–5, with the fixed parameters used in the forward modeling presented in Table 1. Fig. 2 shows the influence of $S_{\rm w}$ and $V_{\rm sh}$ on elastic properties when $\phi=0.1$, $\alpha_{\rm s}=0.12$, and $\alpha_{\rm c}=0.05$; Fig. 3 shows the influence of ϕ and $V_{\rm sh}$ on elastic properties when $S_{\rm w}=0.5$, $\alpha_{\rm s}=0.12$, and $\alpha_{\rm c}=0.05$; Fig. 4 shows the influence of $S_{\rm w}$ and ϕ on elastic properties when $V_{\rm sh}=0.5$, $\alpha_{\rm s}=0.12$, and $\alpha_{\rm c}=0.05$; and Fig. 5 demonstrates the influence of $\alpha_{\rm s}$ and $\alpha_{\rm c}$ on P-wave and S-wave velocities when $\phi=0.1$, $S_{\rm w}=0.5$, and $V_{\rm sh}=0.5$.

From Figs. 2–4, it can be seen that $V_{\rm sh}$ and ϕ have a significant impact on elastic properties, with velocities and densities gradually decreasing as $V_{\rm sh}$ and ϕ increase. On the other hand, $S_{\rm w}$ has a smaller impact, with P-wave and S-wave velocities remaining almost unchanged as $S_{\rm w}$ increases, while density slowly increases. From Fig. 5, it is clear that $\alpha_{\rm s}$ and $\alpha_{\rm c}$ have a considerable influence on P-wave and S-wave velocities, and different combinations of $\alpha_{\rm s}$ and $\alpha_{\rm c}$ lead to significant variations in these velocities. Therefore, in cases where the pore structure is complex, the impact of pore aspect ratios on elastic properties needs to be carefully considered.

Table 1The parameters for rock physics modeling.

Components	Bulk modulus, GPa	Shear modulus, GPa	Density, g/cm ³
Quartz	48	30	2.79
Clay	39	7	2.53
Brine	2	\	1.47
Gas	0.001	\	0.13

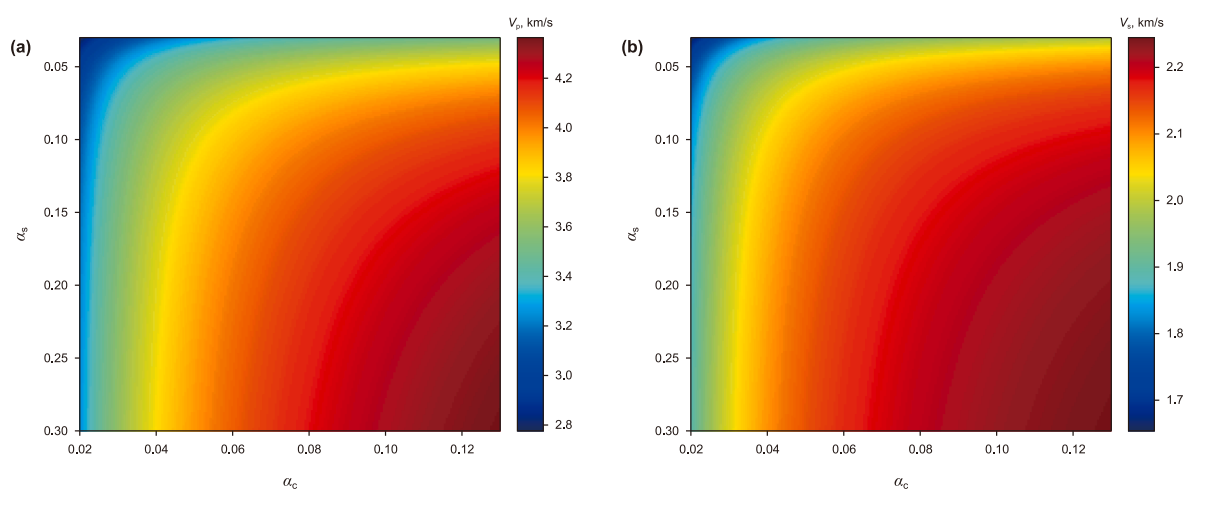


Fig. 5. The influence of α_s and α_c on elastic parameters. (a) The impact of α_s and α_c on V_p . (b) The impact of α_s and α_c on V_s .

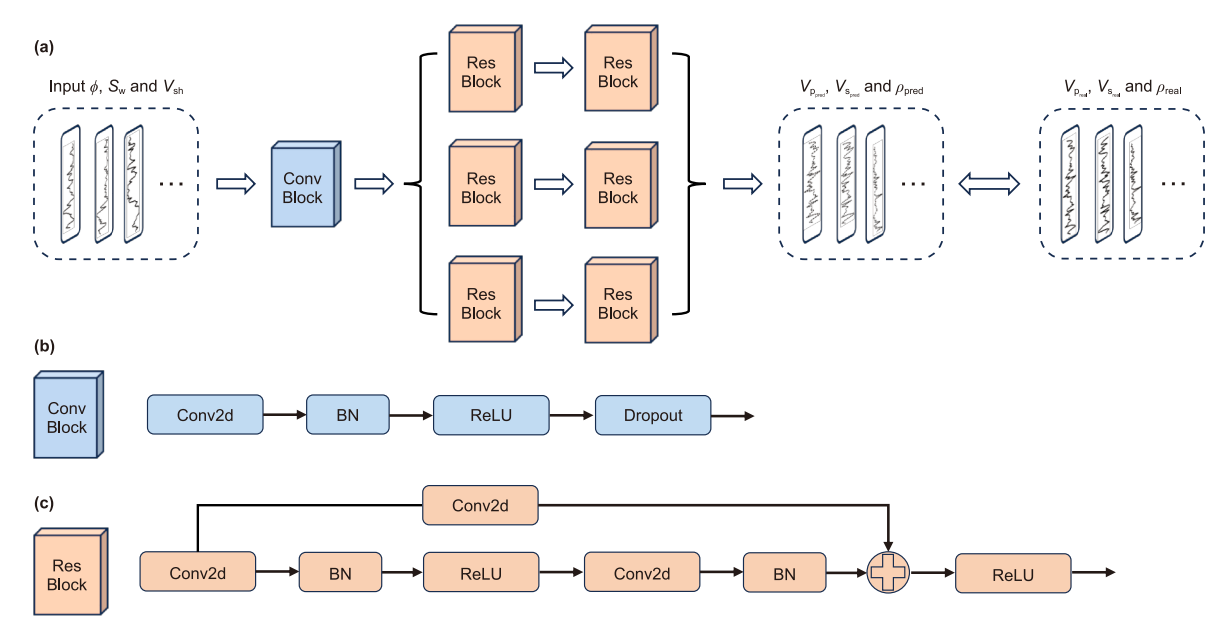


Fig. 6. The process of the RP-Net. (a) The overall framework of the RP-Net. (b) The process of Conv Block. (c) The process of ResBlock.

2.3. RP-Net

To lessen the effects of insufficient real labels and improve the model's capacity for generalization, pseudo labels can be created and added to the training set when genuine labels are hard to come by Lee (2013). Therefore, after completing the rock physics modeling, we generate pseudo reservoir parameters by modifying the existing reservoir parameters and then use these parameters

and the rock physics model to generate pseudo elastic parameters. Fig. 6 shows the construction of the RP-Net, which is trained using both the actual and pseudo parameters. In Fig. 6(a), the real reservoir parameters are combined with the pseudo reservoir parameters as input to the network. The input is processed through a shared convolutional block, followed by two separate residual blocks, to obtain the P-wave velocity, S-wave velocity, and density, respectively. The final output is created by concatenating

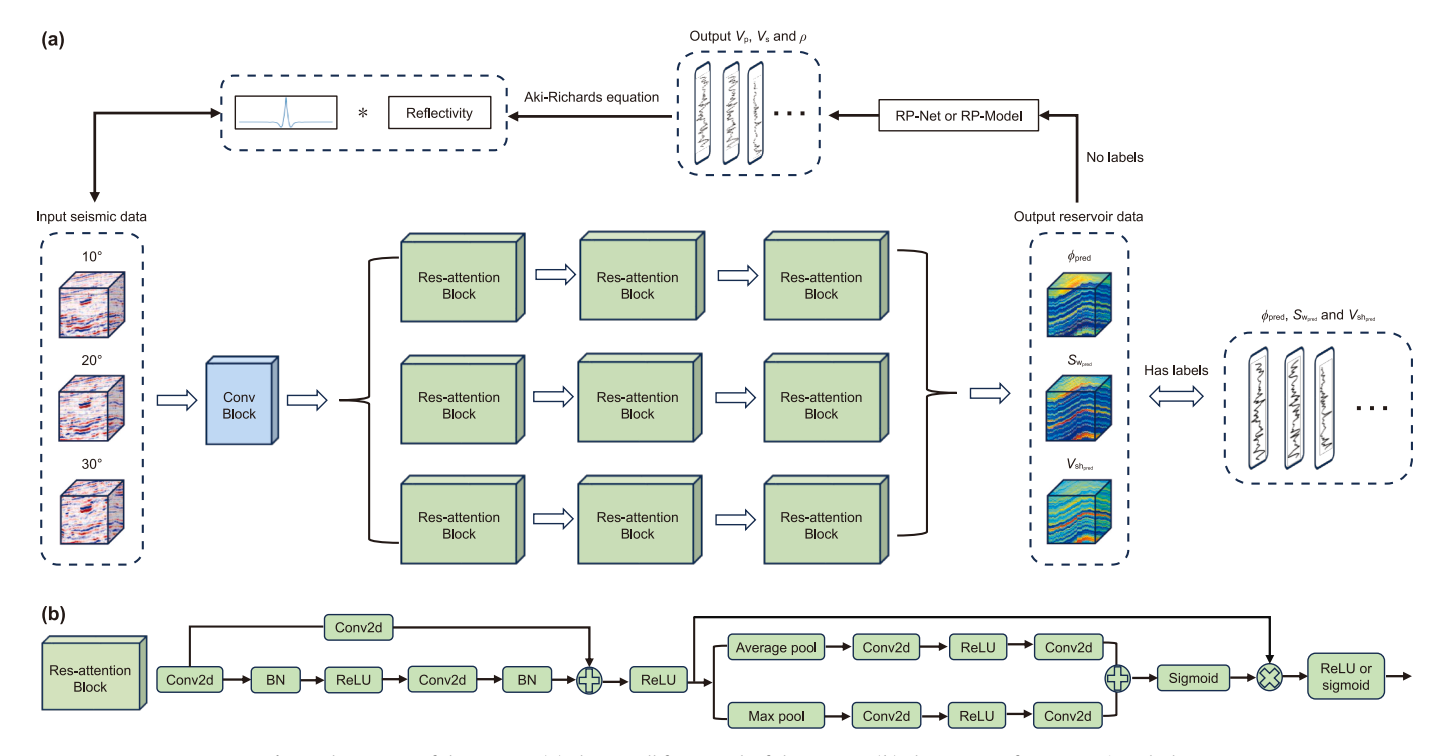


Fig. 7. The process of the Inv-Net. (a) The overall framework of the Inv-Net. (b) The process of Res-Attention Block.

these outputs along the channel dimension. The structures of the convolutional block and the residual block are shown in Fig. 6(b) and (c), respectively. The output is then compared with the corresponding real elastic parameters and pseudo elastic parameters for error analysis to update the network's gradient. The error calculation process can be expressed as:

$$L_{\rm rp}^{1} = \frac{\sum_{i=0}^{n-1} \left[y_{\rm pred}^{1}(i) - y_{\rm real}^{1}(i) \right]^{2}}{\sum_{i=0}^{n-1} \left[y_{\rm real}^{1}(i) \right]^{2}}$$
(21)

$$L_{\rm rp}^2 = \frac{\sum_{i=0}^{n-1} \left[y_{\rm pred}^2(i) - y_{\rm real}^2(i) \right]^2}{\sum_{i=0}^{n-1} \left[y_{\rm real}^2(i) \right]^2}$$
(22)

$$L_{\rm rp} = \alpha L_{\rm rp}^1 + (1 - \alpha) L_{\rm rp}^2 \tag{23}$$

where, $y_{\rm pred}^1$, $y_{\rm real}^1$, and $L_{\rm rp}^1$ represent the output obtained by putting the real reservoir parameters into the network, the real elastic parameters, and the error between them, respectively. Similarly, $y_{\rm pred}^2$, $y_{\rm real}^2$, and $L_{\rm rp}^2$ represent the output obtained by putting the pseudo reservoir parameters into the network, the pseudo elastic parameters, and their error, respectively. n represents the length of the data, and $L_{\rm rp}$ is the total error calculated by weighted summation of $L_{\rm rp}^1$ and $L_{\rm rp}^2$, with α as the weighting factor.

Once the RP-Net is obtained, it can be used to derive the corresponding elastic parameters from the reservoir parameters, as shown in the following equation:

$$E_{\text{Net}}(V_{\text{p}}, V_{\text{s}}, \rho) = \text{Net}^{\text{RP}}(\phi, S_{\text{w}}, V_{\text{sh}})$$
(24)

where, $\operatorname{Net}^{\operatorname{RP}}(\cdot)$ denotes the RP-Net, and $E_{\operatorname{Net}}(\cdot)$ represents the elastic parameters derived through the RP-Net. RP-Net is an essential step in generating synthetic records at the non-well locations, and serves as a bridge between reservoir parameters and elastic parameters. Compared to Eq. (18), RP-Net can to some extent learn parameters such as elastic modulus and pore aspect ratio hidden at non-well locations, thus enabling the conversion of reservoir parameters to elastic parameters without knowing "P".

2.4. Construction of the forward operator

Seismic amplitude can be represented as the convolution of the seismic wavelet and the P-wave reflection coefficient (Robinson, 1985). The specific equation is shown below:

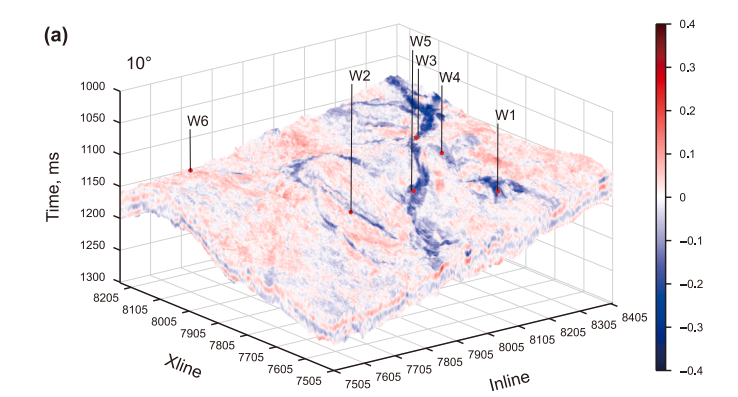
$$d_{\text{cal}} = R_{\text{pp}}(\theta) *W + n \tag{25}$$

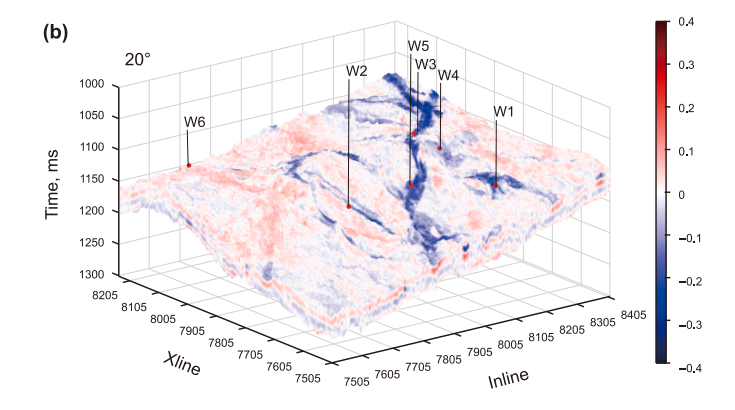
where $d_{\rm cal}$ represents the calculated seismic amplitude, W represents the seismic wavelet, $R_{\rm pp}(\theta)$ represents the P-wave reflection coefficient, n represents noise and errors, and the symbol * represents convolution. The exact equation for the P-wave reflection coefficient is complex, so it is generally replaced by an approximate expression of the Zoeppritz equations. In this paper, the Aki-Richards equation is used as a substitute for the Zoeppritz equations, with the specific equation as follows:

$$R_{pp}(\theta) = \left(\frac{1}{2} + \frac{1}{2}\tan^{2}\theta\right) \frac{\Delta V_{p}}{\overline{V}_{p}} - 4\sin^{2}\theta \frac{\overline{V}_{s}^{2}}{\overline{V}_{p}^{2}} \frac{\Delta V_{s}}{\overline{V}_{s}} + \left(\frac{1}{2} - 2\sin^{2}\theta \frac{\overline{V}_{s}^{2}}{\overline{V}_{p}^{2}}\right) \frac{\Delta \rho}{\overline{\rho}}$$
(26)

where \overline{V}_p , \overline{V}_s , and $\overline{\rho}$ represent the average values of V_p , V_s , and ρ across the upper and lower reflecting interfaces, while ΔV_p , ΔV_s , and $\Delta \rho$ represent the differences in V_p , V_s , and ρ between the interfaces, and θ represents the incident angle.

By combining Eqs. (24)–(26), a forward operator linking reservoir parameters to seismic amplitude can be constructed, as shown in the following equation:





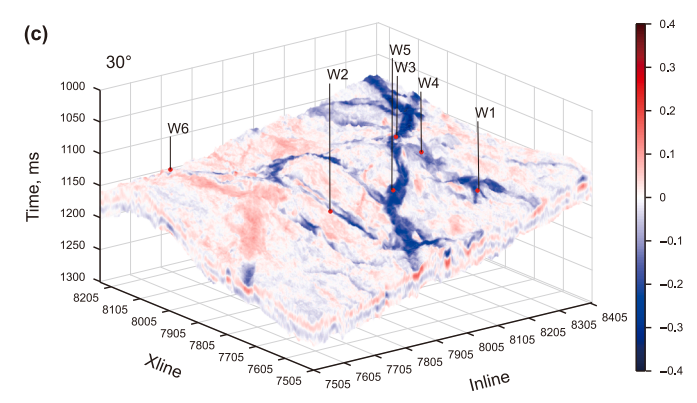


Fig. 8. Seismic data volume. **(a)** The small-angle seismic stacks with an average angle of 10°. **(b)** The middle-angle seismic stacks with an average angle of 20°. **(c)** The large-angle seismic stacks with an average angle of 30°.

$$d_{\text{cal}} = F(\theta, \phi, S_{\text{W}}, V_{\text{sh}}, W, n) \tag{27}$$

where $F(\cdot)$ represents the forward operator, which is highly nonlinear. Therefore, in this paper, an inversion network is designed to directly invert reservoir parameters from seismic data.

2.5. Inv-Net

The Inv-Net designed in this paper is shown in Fig. 7. The network includes a convolutional block (as shown in Fig. 6(b)) and three Res-Attention blocks (as shown in Fig. 7(b)). A channel attention mechanism and a residual component make up each Res-Attention block. Through max-pooling and average-pooling, the channel attention mechanism dynamically weights the feature channels, improving the model's performance by helping it better learn significant feature representations (Hu et al., 2019; Woo et al., 2018). Three sets of stacked seismic data—corresponding to small-angle stacks with an average angle of 10°, medium-angle stacks with an average angle of 30°—combine to provide the network's input. The three Res-Attention blocks come after the convolutional block, which produces the predicted reservoir parameters.

The following equation is used to determine the error between the predicted and real reservoir parameters for well locations where real reservoir parameters are available:

$$L_{\text{inv}}^{1} = \frac{\sum_{i=0}^{n-1} \left[m_{\text{pred}}(i) - m_{\text{real}}(i) \right]^{2}}{\sum_{i=0}^{n-1} \left[m_{\text{real}}(i) \right]^{2}}$$
(28)

The predicted reservoir parameters are entered into Eq. (27) to

create synthetic seismic data for locations where real reservoir parameters are not accessible. The discrepancy between this synthetic data and the corresponding real seismic data is then calculated. The calculation is shown in the following equation:

$$L_{\text{inv}}^{2} = \frac{1}{2} \left(1 - \frac{\sum_{i=0}^{n-1} (d_{\text{cal}}(i) - \overline{d}_{\text{cal}}) (d_{\text{real}}(i) - \overline{d}_{\text{real}})}{\sqrt{\sum_{i=0}^{n-1} (d_{\text{cal}}(i) - \overline{d}_{\text{cal}})^{2}} \sqrt{\sum_{i=0}^{n-1} (d_{\text{real}}(i) - \overline{d}_{\text{real}})^{2}}} \right)$$
(29)

Then, $L_{\rm inv}^1$ and $L_{\rm inv}^2$ are combined with a weighted sum to obtain the total error $L_{\rm inv}$, as shown in the following equation:

$$L_{\text{inv}} = \beta L_{\text{inv}}^{1} + (1 - \beta) L_{\text{inv}}^{2}$$
 (30)

where m_{pred} and m_{real} represent the predicted and actual reservoir parameters, d_{cal} and $\overline{d}_{\mathrm{cal}}$ represent the synthetic seismic data and its mean, and d_{real} and $\overline{d}_{\mathrm{real}}$ represent the actual seismic data and its mean. L^1_{inv} , L^2_{inv} , and L_{inv} represent the errors at well locations, non-well locations, and the total error, respectively, with β denoting the weight coefficient.

3. Results

To validate the effectiveness and feasibility of the proposed RP-Net and Inv-Net, actual data from a work area in southwestern China was used for testing. The selected work area mainly features fluvial deposits with multiple stages of channel development. The lithology consists of purple-red mudstone interbedded with sandstone, and the target interval is primarily a tight sandstone reservoir. The area is covered by a 3D pre-stack seismic dataset

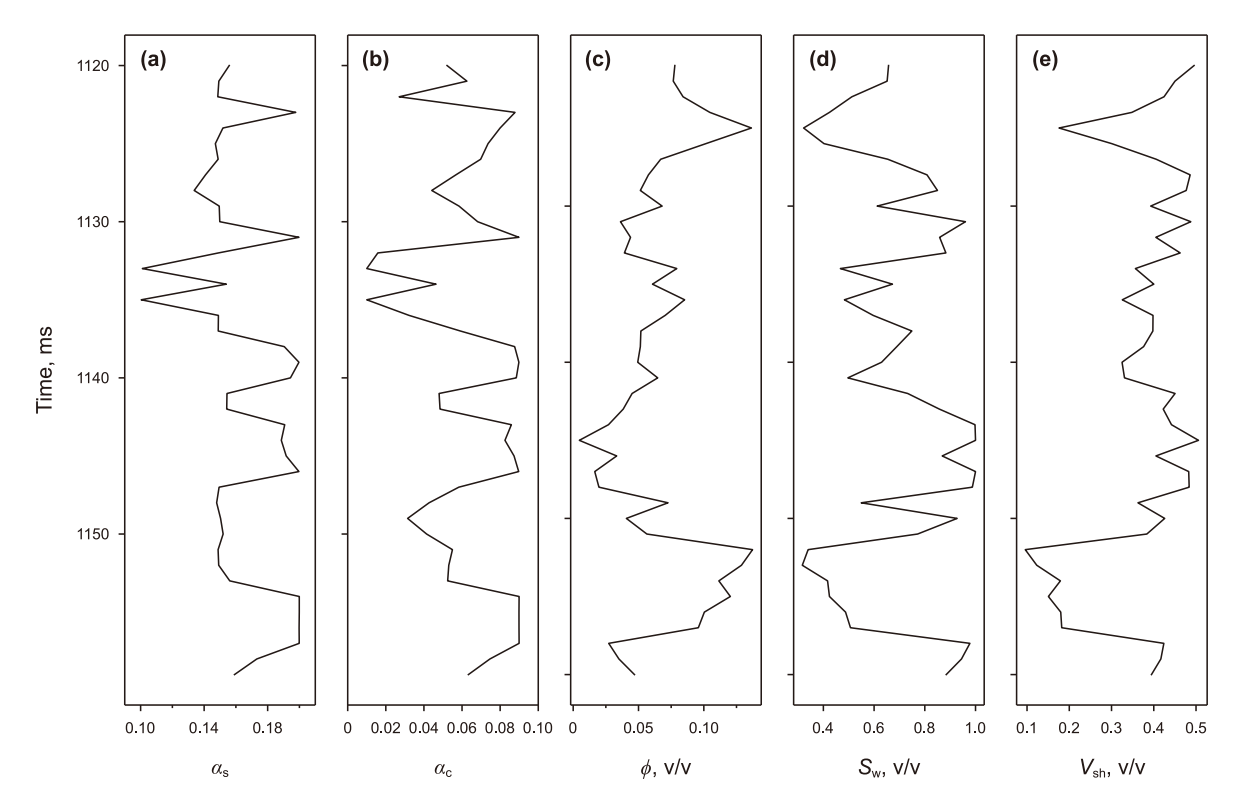


Fig. 9. Reservoir parameters used in rock physics modeling. **(a)** The pore aspect ratio of sand α_s used. **(b)** The pore aspect ratio of clay α_c used. **(c)** The ϕ used. **(d)** The S_w used. **(e)** The V_{sh} used.

with horizon constraints, including six wells. The dataset contains 906 traces in the Inline direction and 738 traces in the xline direction, as shown in Fig. 8.

We first perform rock physics modeling using the reservoir parameters at the wells, the parameters in Table 1, and Eqs. (1)–(18). The pore aspect ratio used in the modeling was estimated using Eq. (19), and the optimization algorithm was "trust-constr". The initial value for the sandstone pore aspect ratio was obtained from Eq. (20), with a search range from 0.1 to 0.2, while the initial value for the mudstone pore aspect ratio was set to 0.05, with a search range from 0.01 to 0.1. Fig. 9 shows the reservoir parameters and pore aspect ratios for Well 1 during modeling, and Fig. 10 presents the modeled elastic parameters compared to the actual elastic parameters. As can be seen, the modeled elastic parameters closely match the actual ones, indicating that the applied rock physics model is both effective and feasible.

Next, we simulate the reservoir parameters of five wells (Well 1 to Well 5) in the work area. We create 10 sets of pseudo porosity curves, 4 sets of pseudo water saturation curves, and 4 sets of pseudo clay volume curves based on the real reservoir data of each well. This results in 800 sets ($5 \times 10 \times 4 \times 4$) of pseudo reservoir parameter curves, as indicated in Table 2. Then, using these pseudo reservoir parameters and the constructed rock physics model, we calculate the pseudo elastic parameters. We use Well 6 as a blind well to test the efficacy of the network after combining the real and pseudo parameters to train the RP-Net. The hyperparameters used in the training are listed in Table 3, and the optimization

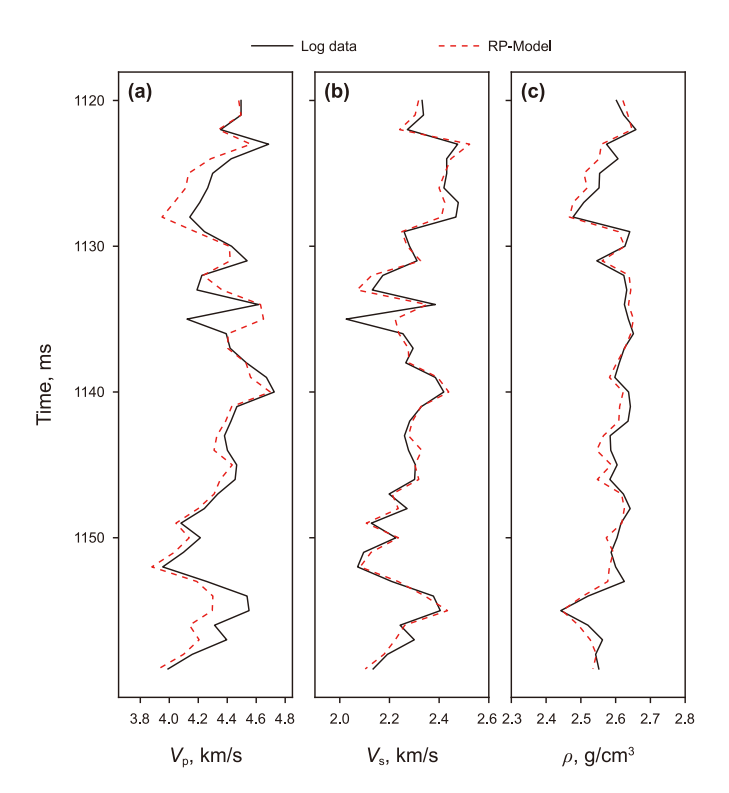


Fig. 10. Comparison between the elastic parameters obtained from rock physics forward modeling (red line) and the actual elastic parameters (black line) at Well 1. (a) The comparison of the built V_p and the actual V_p . (b) The comparison of the built V_s and the actual V_s . (c) The comparison of the built ρ and the actual ρ .

Table 2The generation process of pseudo reservoir parameters.

Components	Pseudo data			Number	
$\phi S_{ m W} V_{ m sh}$	$\phi + 0.5\%$	$\phi + 1\%$		$\phi + 5\%$	10 in total
	$S_w - 5\%$	$S_W - 10\%$	S _w - 15%	$S_{w} - 20\%$	4 in total
	$V_{sh} + 3\%$	$V_{sh} + 6\%$	V _{sh} + 9%	$V_{sh} + 12\%$	4 in total

Table 3 Parameters used in the RP-Net.

	Learning rate	Weight decay	Batch size	α
Value	0.008	1e-5	10	0.75

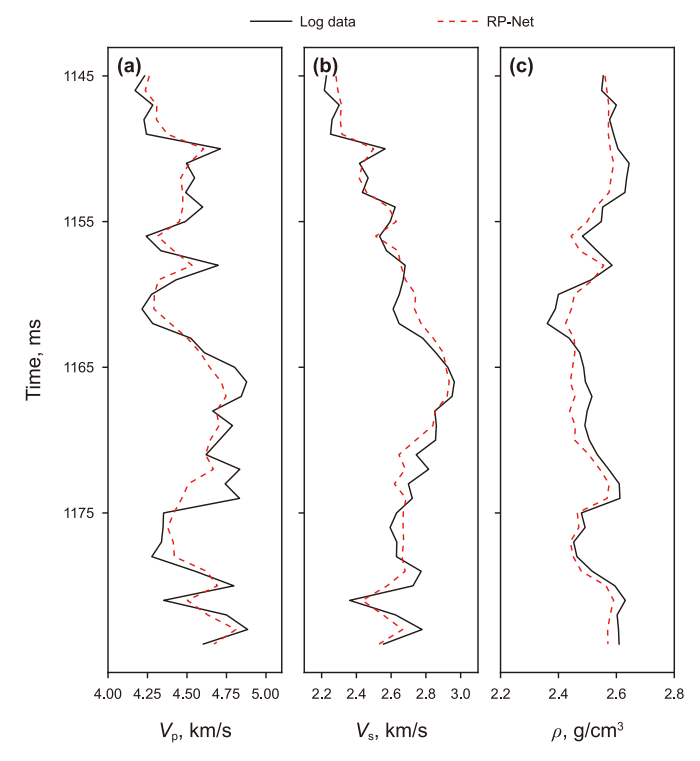


Fig. 11. The elastic parameters predicted by the RP-Net (red line) and the actual elastic parameters (black line) at the blind well. **(a)** The comparison of the predicted V_p and the actual V_p . **(b)** The comparison of the predicted V_s and the actual V_s . **(c)** The comparison of the predicted ρ and the actual ρ .

algorithm is Adam. Fig. 11 shows the prediction performance at the blind well. The viability of the network is demonstrated by the observation that the predicted elastic parameters at the blind well roughly match the actual elastic parameters.

Table 4 Parameters used in the Inv-Net.

	Learning rate	Weight decay	Batch size	β
Value	0.008	1e-4	60	0.95

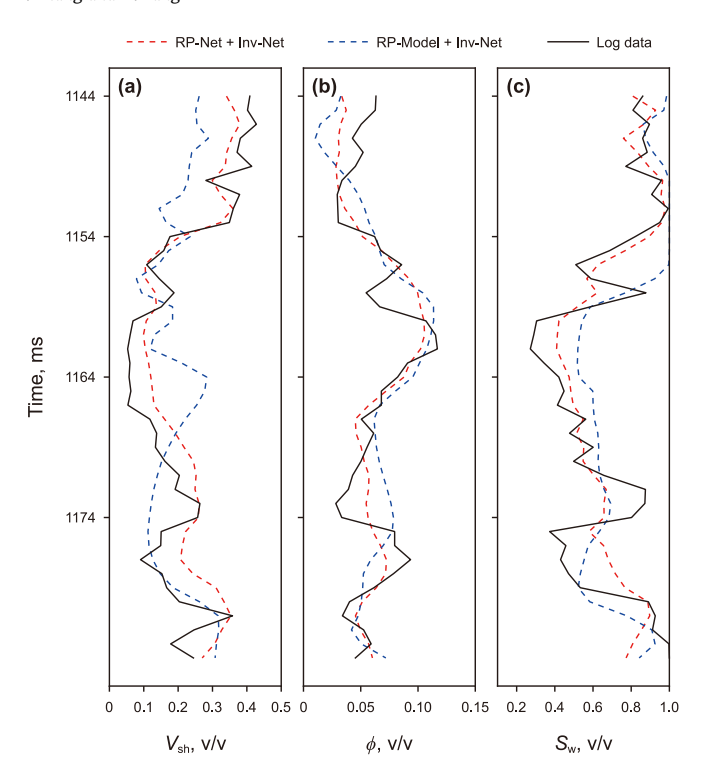


Fig. 12. The reservoir parameters predicted by the "RP-Net + Inv-Net" (red line) the "RP-Model + Inv-Net" (blue line) and the actual reservoir parameters (black line) at the blind well. **(a)** The comparison of the predicted $V_{\rm sh}$ and the actual $V_{\rm sh}$. **(b)** The comparison of the predicted $V_{\rm sh}$ and the actual $V_{\rm sh}$.

We use the seismic data as input to train the Inv-Net after integrating the trained RP-Net into the network depicted in Fig. 7. To confirm the efficacy of the network, we employed Well 6 as a blind well and Adam as the optimization algorithm. The hyperparameters used during training are listed in Table 4. The parameter "P" (in Eq. (18)) used in "RP-Model + Inv-Net" is shown in Table 1 and Fig. 9(a) and (b). The inversion results at the blind well are shown in Fig. 12 and Table 5, while the seismic profile and inversion result profile along the xline at the blind well are shown in Figs. 13 and 14, respectively. The seismic profile and inversion result profile along the Inline at the blind well are shown in Figs. 15 and 16, respectively. The 2D slice of the maximum predicted, the minimum predicted $S_{\rm W}$ and $V_{\rm sh}$ along the time axis are shown in Figs. 17–19.

From Fig. 12 and Table 5, the reservoir parameters obtained by "RP-Net + Inv-Net" have a higher correlation with the actual

Table 5The correlation coefficient and MSE between the inversion result and the actual log curve.

Index	Method	$V_{\rm sh}$, v/v	ϕ , v/v	S_w , v/v
Correlation coefficient	RP-Net + Inv-Net	0.8785	0.7812	0.7834
	RP-Model + Inv-Net	0.3140	0.5566	0.7276
MSE	RP-Net + Inv-Net	0.0041	0.0003	0.0205
	$RP ext{-}Model + Inv ext{-}Net$	0.0135	0.0006	0.0305

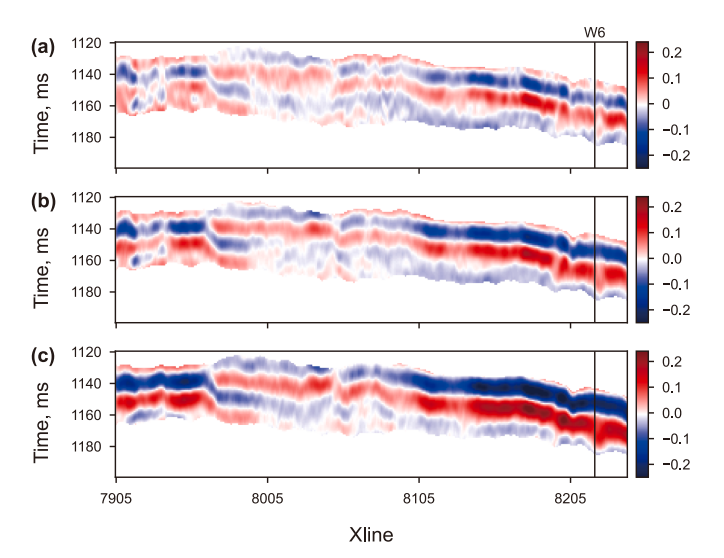


Fig. 13. Seismic profile along the xline direction at the blind well. (a) The small-angle seismic stacks with an average angle of 10°. (b) The middle-angle seismic stacks with an average angle of 20°. (c) The large-angle seismic stacks with an average angle of 30°.

reservoir parameters and smaller errors than those obtained by "RP-Model + Inv-Net". From Figs. 13–19, compared to "RP-Model + Inv-Net", the results obtained by "RP-Net + Inv-Net" have better lateral continuity and better hierarchical relationship from lithology, physical property to gas-bearing property. In addition, the predicted 2D slices by "RP-Net + Inv-Net" effectively illustrate the orientation and distribution of sedimentary channels, aiding in the selection of well placements.

4. Discussion

Most current seismic reservoir parameter inversion methods rely on 2D seismic data, which is unable to adequately guide well location selection since it does not give complete attribute information for the whole work area. Furthermore, these methods frequently depend on algorithms—like inversion algorithms based on Bayesian theory—which adds complexity to the computation. Building on previous research, this paper proposes an intelligent method using deep learning to directly invert reservoir parameters from 3D seismic data. The inversion results obtained from this method can reveal the direction and distribution of the depositional channels in the selected work area, which is helpful for well location selection and indicating gasbearing zones.

However, there are some drawbacks to this study. The proposed Inv-Net, firstly, is sensitive to certain hyperparameters (such as learning rate and regularization parameters), and there is still insufficient theoretical support for choosing the appropriate values for these hyperparameters. Therefore, achieving optimal inversion results necessitates careful tuning of some hyperparameters in the network or using automatic tuning tools to find suitable combinations. Secondly, it is possible that the network trained in this study would not generalize well to work locations where the depositional environment is different from the one that was chosen. Thus, for other work areas, it may

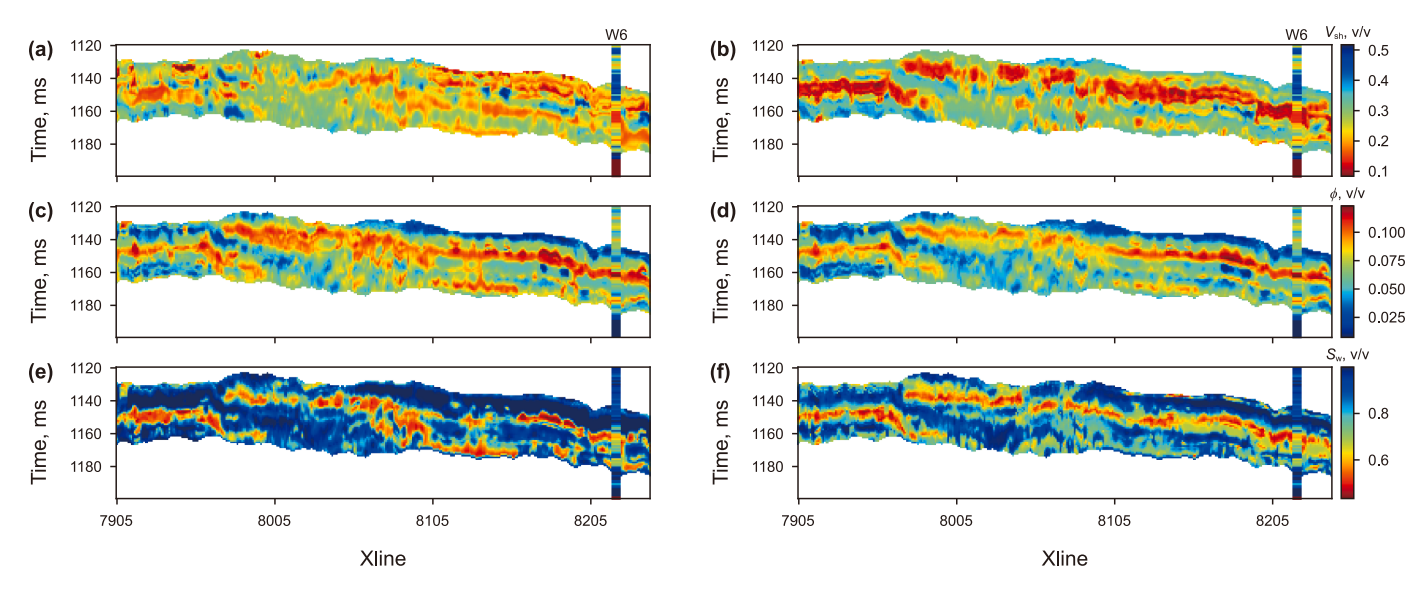


Fig. 14. The inversion result profile along the xline direction at the blind well. (a) The predicted $V_{\rm sh}$ by "RP-Model + Inv-Net". (b) The predicted $V_{\rm sh}$ by "RP-Net + Inv-Net". (c) The predicted ϕ by "RP-Model + Inv-Net". (d) The predicted ϕ by "RP-Net + Inv-Net". (e) The predicted $S_{\rm w}$ by "RP-Model + Inv-Net". (f) The predicted $S_{\rm w}$ by "RP-Net + Inv-Net".

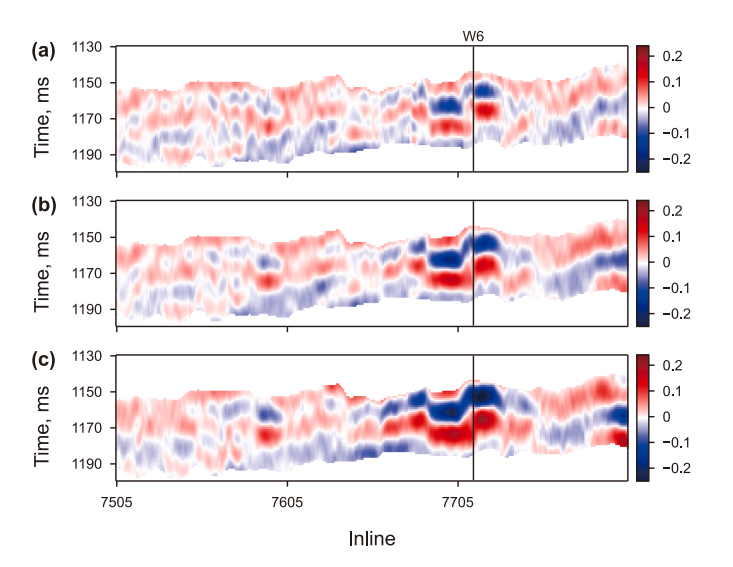


Fig. 15. Seismic profile along the Inline direction at the blind well. (a) The small-angle seismic stacks with an average angle of 10°. (b) The middle-angle seismic stacks with an average angle of 20°. (c) The large-angle seismic stacks with an average angle of 30°.

be necessary to retrain a new network using seismic and well data from the specific area. Thirdly, the nonlinear relationship between the reservoir parameters and the corresponding seismic data in the selected work area is highly complex, and the seismic data is affected by noise, leading to a relatively low

signal-to-noise ratio. As a result, the resolution of the inverted seismic sections may not be as high as expected. Fourth, the rock physics models used in this paper (such as the Gassmann equation) involve many theoretical assumptions, and anisotropy within the rock was not considered during modeling, which may cause discrepancies between the modeled elastic parameters and the corresponding actual well log curves. Lastly, like most intelligent inversion methods, the proposed method carries a risk of overfitting to some extent. In future work, we will focus on addressing these issues.

5. Conclusion

In this study, we proposed an intelligent method to directly invert porosity, clay content, and water saturation from 3D seismic data. The method uses a rock physics model that considers variable pore aspect ratios to generate pseudo data, which are then combined with actual data to train a rock physics network. We incorporated this rock physics network with the Aki-Richards equation to build a forward operator that links reservoir parameters to seismic data. Using this forward operator, along with an inversion network, we achieved the direct inversion of reservoir parameters from 3D seismic data. To verify the feasibility of the proposed method, we tested it using real seismic data from a tight gas-bearing sandstone formation in Southwest China. The results show that the inversion results at the blind well match well with the actual data, and the inverted profiles and slices effectively indicate the lithology and gas-bearing properties of the selected work area, realizing a quantitative prediction of reservoir parameters for this region.

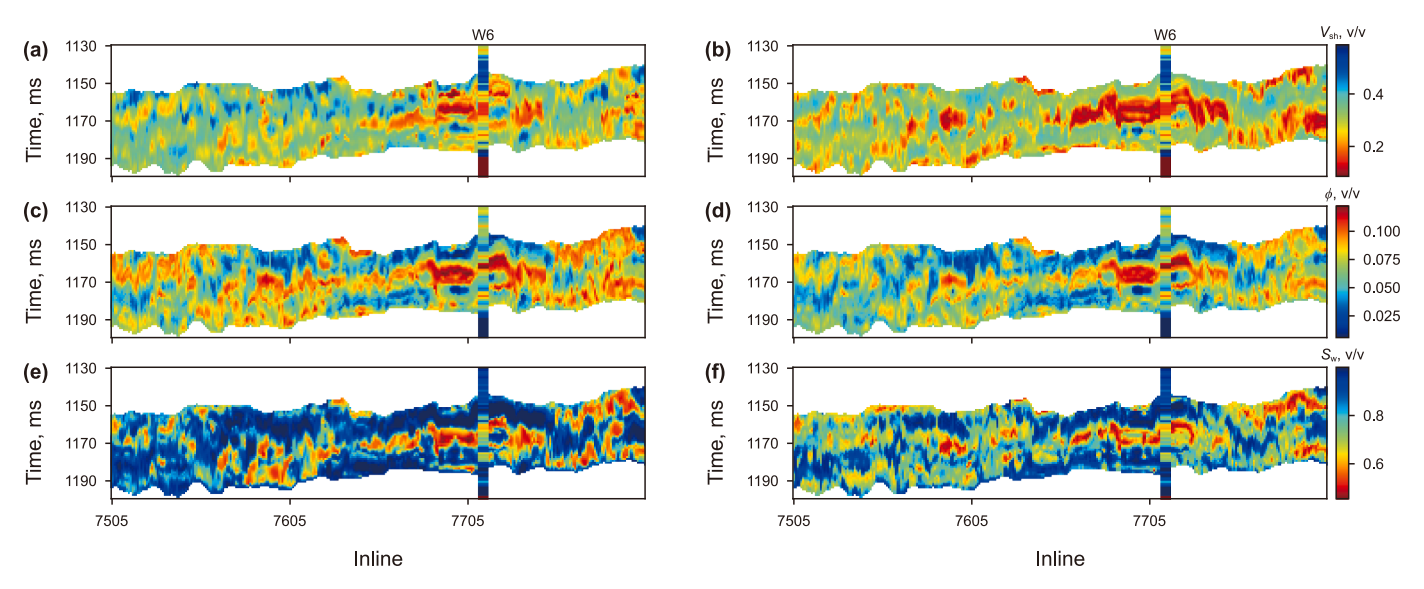


Fig. 16. The inversion result profile along the Inline direction at the blind well. **(a)** The predicted $V_{\rm sh}$ by "RP-Model + Inv-Net". **(b)** The predicted $V_{\rm sh}$ by "RP-Net + Inv-Net". **(c)** The predicted ϕ by "RP-Model + Inv-Net". **(d)** The predicted ϕ by "RP-Net + Inv-Net". **(e)** The predicted $S_{\rm w}$ by "RP-Model + Inv-Net". **(f)** The predicted $S_{\rm w}$ by "RP-Net + Inv-Net".

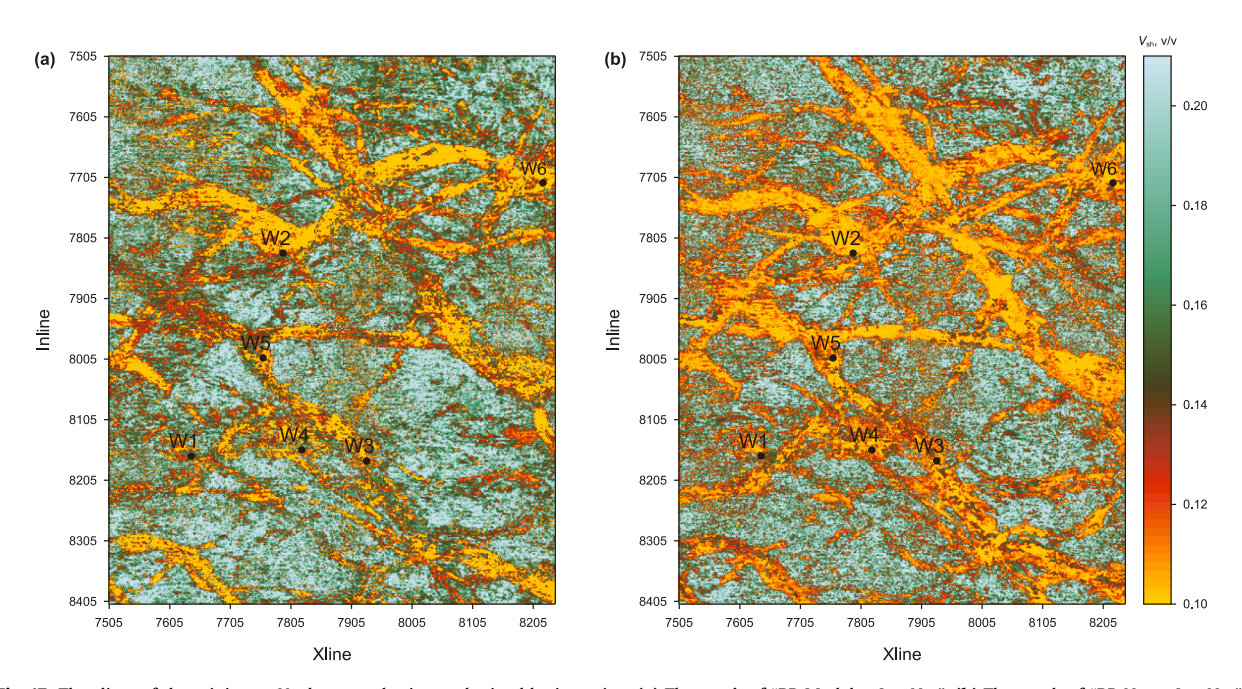


Fig. 17. The slices of the minimum V_{sh} between horizons obtained by inversion. (a) The result of "RP-Model + Inv-Net". (b) The result of "RP-Net + Inv-Net".

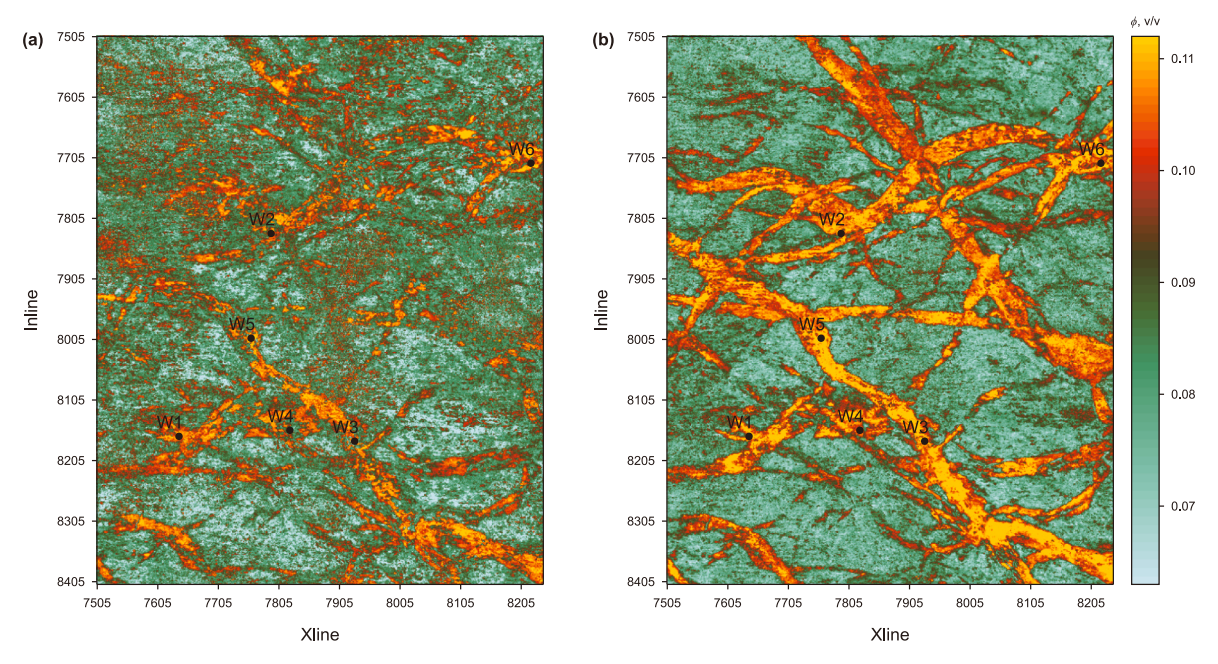


Fig. 18. The slices of the maximum ϕ between horizons obtained by inversion. (a) The result of "RP-Model + Inv-Net". (b) The result of "RP-Net + Inv-Net".

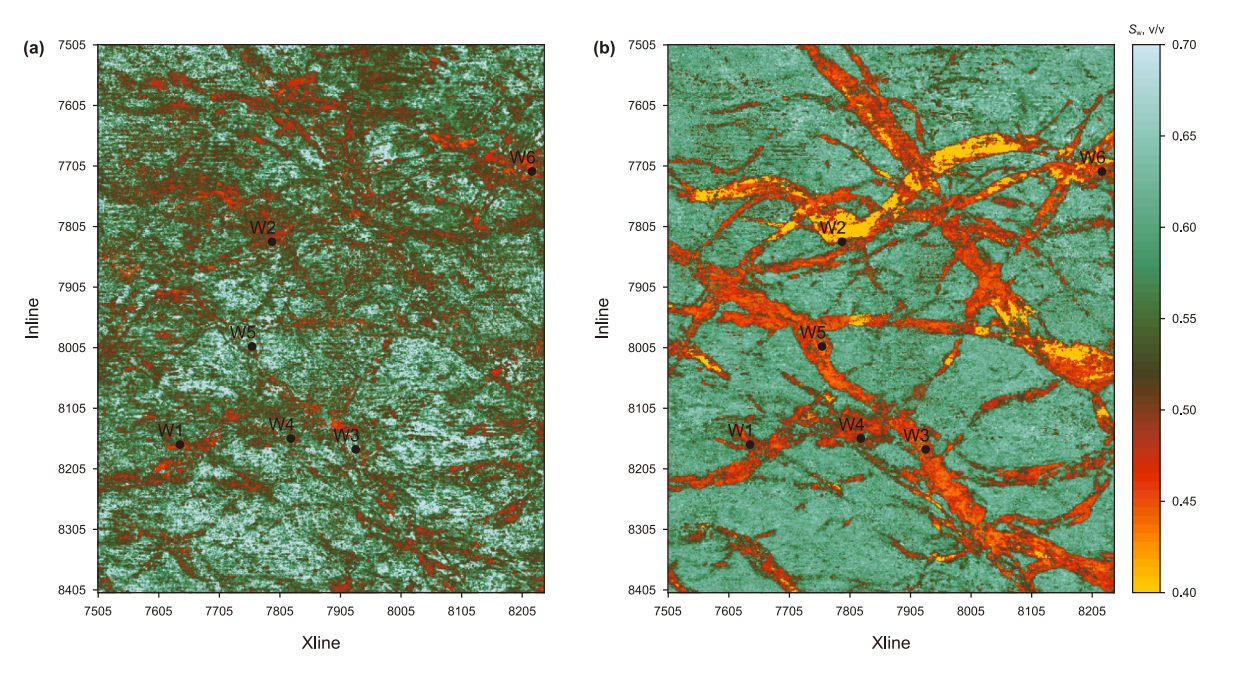


Fig. 19. The slices of the minimum S_W between horizons obtained by inversion. (a) The result of "RP-Model + Inv-Net". (b) The result of "RP-Net + Inv-Net".

CRediT authorship contribution statement

Yang Zhang: Writing – review & editing, Writing – original draft, Validation, Software, Methodology, Data curation, Conceptualization. **Hao Yang:** Resources, Project administration, Investigation, Funding acquisition, Data curation, Conceptualization.

Declaration of competing interest

The authors declare that they have no known competing financial interests or personal relationships that could have appeared to influence the work reported in this paper.

Acknowledgements

The authors thank the supports provided by "the CNPC Science and Technology Major Project (Grant Nos. 2023ZZ05, 2023ZZ05-05, 2023ZZ18-03) and Changqing Oilfield Science and Technology Major Project (Grant No. 2023DZZ01)".

Appendix A

$$T_{iijj}(\alpha) = \frac{3F_1}{F_2} \tag{A.1}$$

$$F(\alpha) = \frac{2}{F_3} + \frac{1}{F_4} + \frac{F_4 F_5 + F_6 F_7 - F_8 F_9}{F_2 F_4}$$
(A.2)

$$F_1 = 1 + A \left[\frac{3}{2} (g+h) - R \left(\frac{3}{2} g + \frac{5}{2} h - \frac{4}{3} \right) \right]$$
 (A.3)

$$F_2 = 1 + A \left[1 + \frac{3}{2}(g+h) - \frac{R}{2}(3g+5h) \right] + B(3-4R)$$
 (A.4)

$$+\frac{A}{2}(A+3B)(3-4R)\left[g+h-R\left(g-h+2h^{2}\right)\right]$$
 (A.5)

$$F_3 = 1 + \frac{A}{2} \left[R(2-h) + \frac{(1+\alpha^2)}{\alpha^2} h(R-1) \right]$$
 (A.6)

$$F_4 = 1 + \frac{A}{4} [3h + g - R(g - h)] \tag{A.7}$$

$$F_5 = A \left[R \left(g + h - \frac{4}{3} \right) - g \right] + Bh(3 - 4R)$$
 (A.8)

$$F_6 = 1 + A[1 + g - R(g + h)] + B(1 - h)(3 - 4R)$$
(A.9)

$$F_7 = 2 + \frac{A}{4} [9h + 3g - R(5h + 3g)] + Bh(3 - 4R)$$
 (A.10)

$$F_8 = A \left[1 - 2R + \frac{g}{2}(R - 1) + \frac{h}{2}(5R - 3) \right] + B(1 - h)(3 - 4R)$$
(A.11)

$$F_9 = A[g(R-1) - R h] + B h(3-4R)$$
(A.12)

$$A = \frac{\mu^*}{\mu_{\rm m}} - 1, B = \frac{1}{3} \left(\frac{K^*}{K_{\rm m}} - \frac{\mu^*}{\mu_{\rm m}} \right) R = \frac{3\mu_{\rm m}}{3K_{\rm m} + 4\mu_{\rm m}}$$
(A.13)

$$h = \frac{\alpha}{(1 - \alpha^2)^{\frac{3}{2}}} \left[\cos^{-1} \alpha - \alpha \left(1 - \alpha^2 \right)^{\frac{1}{2}} \right]$$
 (A.14)

$$g = \frac{a^2}{1 - a^2} (3h - 2) \tag{A.15}$$

References

Aki, K., Richards, P.G., 2009. Quantitative Seismology, second ed. University Science Books. New York.

Aleardi, M., Ciabarri, F., Mazzotti, A., 2017. Probabilistic estimation of reservoir properties by means of wide-angle AVA inversion and a petrophysical reformulation of the Zoeppritz equations. J. Appl. Geophys. 147, 28–41. https://doi. org/10.1016/j.jappgeo.2017.10.002.

Alfarraj, M., AlRegib, G., 2019. Semi-supervised sequence modeling for elastic impedance inversion. Interpretation 7 (3), SE237–SE249. https://doi.org/ 10.1190/INT-2018-0250.1.

Ba, J., Xu, W., Fu, L.Y., et al., 2017. Rock anelasticity due to patchy saturation and fabric heterogeneity: a double double-porosity model of wave propagation. J. Geophys. Res. Solid Earth 122 (3), 1949–1976. https://doi.org/10.1002/2016IR013882

Bachrach, R., 2006. Joint estimation of porosity and saturation using stochastic rock-physics modeling. Geophysics 71 (5), 053–063. https://doi.org/10.1190/ 1.2235991.

Berryman, J.G., 1980. Long-wavelength propagation in composite elastic media I. Spherical inclusions. J. Acoust. Soc. Am. 68 (6), 1809–1819. https://doi.org/10.1121/1.385171.

Biswas, R., Sen, M.K., Das, V., et al., 2019. Prestack and poststack inversion using a physics-guided convolutional neural network. Interpretation 7 (3), SE161–SE174. https://doi.org/10.1190/INT-2018-0236.1.

Bosch, M., Mukerji, T., Gonzalez, E.F., 2010. Seismic inversion for reservoir properties combining statistical rock physics and geostatistics: A review. Geophysics 75 (5), 75A165–75A176. https://doi.org/10.1190/1.3478209.

Buland, A., Omre, H., 2003. Bayesian linearized AVO inversion. Geophysics 68 (1), 185–198. https://doi.org/10.1190/1.1543206.

Chiappa, F., Mazzotti, A., 2009. Estimation of petrophysical parameters by linearized inversion of angle domain pre-stack data. Geophys. Prospect. 57 (3), 413–426. https://doi.org/10.1111/j.1365-2478.2008.00742.x.

Das, V., Mukerji, T., 2020. Petrophysical properties prediction from prestack seismic data using convolutional neural networks. Geophysics 85 (5), N41–N55. https://doi.org/10.1190/geo2019-0650.1.

Das, V., Pollack, A., Wollner, U., Mukerji, T., 2018. Convolutional neural network for seismic impedance inversion. Geophysics 84 (6), R869–R880. https://doi.org/ 10.1190/geo2018-0838.1.

Diakogiannis, F.I., Waldner, F., Caccetta, P., et al., 2020. ResUNet-a: a deep learning framework for semantic segmentation of remotely sensed data. ISPRS. J. Photogramm. Remote. Sens. 162, 94–114. https://doi.org/10.1016/j.isprsjprs.2020.01.013.

Gassmann, F., 1951. Elastic waves through a packing of spheres. Geophysics 16 (4), 673–685. https://doi.org/10.1190/1.1437718.

Goodfellow, I., Pouget-Abadie, J., Mirza, M., et al., 2020. Generative adversarial networks. Commun. ACM 63, 139–144. https://doi.org/10.1145/3422622.

Grana, D., 2016. Bayesian linearized rock-physics inversion. Geophysics 81 (6), D625–D641. https://doi.org/10.1190/geo.2016-0161.1.

Grana, D., Azevedo, L., Figueiredo, L., et al., 2022. Probabilistic inversion of seismic data for reservoir petrophysical characterization: review and examples. Geophysics 87 (5), M199–M216. https://doi.org/10.1190/geo2021-0776.1.

Grana, D., Rossa, E., 2010. Probabilistic petrophysical-properties estimation integrating statistical rock physics with seismic inversion. Geophysics 75 (3), 021–037. https://doi.org/10.1190/1.3386676.

Guo, Q., Ba, J., Carcione, J.M., 2022. Multi-objective petrophysical seismic inversion based on the double-porosity biot–Rayleigh model. Surv. Geophys. 43 (4), 1117–1141. https://doi.org/10.1007/s10712-022-09692-6.

He, K., Zhang, X., Ren, S., et al., 2016. Identity mappings in deep residual networks.

He, K., Zhang, X., Ren, S., et al., 2016. Identity mappings in deep residual networks. In: Computer Vision – ECCV 2016, pp. 630–645. https://doi.org/10.1007/978-3-319-46493-0_38.

He, K., Zhang, X., Ren, S., et al., 2015. Deep residual learning for image recognition. In: Proceedings of the IEEE Conference on Computer Vision and Pattern Recognition (CVPR), pp. 770–778. https://doi.org/10.1109/CVPR.2016.90.

Hill, R., 1952. The elastic behavior of a crystalline aggregate. Proc. Phys. Soc. 65 (5), 349–354. https://doi.org/10.1088/0370-1298/65/5/307.

Hu, J., Shen, L., Albanie, S., et al., 2019. Squeeze-and-Excitation networks. In: Proceedings of the IEEE Conference on Computer Vision and Pattern Recognition, pp. 7132–7141. https://doi.org/10.1109/CVPR.2018.00745.

Huang, G., Liu, Z., van der Maaten, L., et al., 2018. Densely connected convolutional networks. In: Proceedings of the IEEE Conference on Computer Vision and Pattern Recognition, pp. 4700–4708. https://doi.org/10.1109/CVPR.2017.243.

Jiang, M., Spikes, K.T., 2016. Rock-physics and seismic-inversion based reservoir characterization of the Haynesville Shale. J. Geophys. Eng. 13 (3), 220–233. https://doi.org/10.1088/1742-2132/13/3/220.

Junhwan, C., Seokmin, O., Joongmoo, B., 2022. Uncertainty estimation in AVO inversion using Bayesian dropout based deep learning. J. Pet. Sci. Eng. 208, 109288. https://doi.org/10.1016/j.petrol.2021.109288.

- Keys, R.G., Xu, S., 2002. An approximation for the Xu-White velocity model. Geophysics 67 (5), 1406–1414. https://doi.org/10.1190/1.1512786.
- Kuster, G.T., Toksöz, M.N., 1974. Velocity and attenuation of seismic waves in two-phase media: Part I. Theoretical formulations. Geophysics 39 (5), 587–606. https://doi.org/10.1190/1.1440450.
- Lee, D.H., 2013. Pseudo-label: the simple and efficient semi-supervised learning method for deep neural networks. In: Workshop on Challenges in Representation Learning.
- Leite, E.P., Vidal, A.C., 2011. 3D porosity prediction from seismic inversion and neural networks. Comput. Geosci. 37 (8), 1174–1180. https://doi.org/10.1016/j.cageo.2010.08.001.
- Li, K., Yin, X., Zong, Z., 2020. Facies-constrained prestack seismic probabilistic inversion driven by rock physics. Sci. China Earth Sci. 63 (6), 822–840. https:// doi.org/10.1007/s11430-019-9578-1.
- Long, J., Shelhamer, E., Darrell, T., 2015. Fully convolutional networks for semantic segmentation. In: IEEE Transactions on Pattern Analysis and Machine Intelligence, pp. 640–651. https://doi.org/10.1109/TPAMI.2016.2572683.
- Luo, C., Li, X., Huang, G., 2019. Pre-stack AVA inversion by using propagator matrix forward modeling. Pure Appl. Geophys. 176 (10), 4445–4476. https://doi.org/ 10.1007/s00024-019-02157-9.
- Luo, Y., Huang, H., Jakobsen, M., et al., 2019. Prediction of porosity and gas saturation for deep-buried sandstone reservoirs from seismic data using an improved rock-physics model. Acta Geophys. 67, 557–575. https://doi.org/10.1007/s11600-019-00274-6.
- Pan, X., Zhang, G., 2019. Bayesian seismic inversion for estimating fluid content and fracture parameters in a gas-saturated fractured porous reservoir. Sci. China Earth Sci. 62, 798–811. https://doi.org/10.1007/s11430-018-9284-2.
- Pan, X., Zhang, G., Yin, X., 2017. Azimuthally anisotropic elastic impedance inversion for fluid indicator driven by rock physics. Geophysics 82 (6), C211–C227. https://doi.org/10.1190/geo2017-0191.1.
- Reuss, A., 1929. Berechnung der Fließgrenze von Mischkristallen auf Grund der Plastizitätsbedingung für Einkristalle. Z. Angew. Math. Mech. 9 (1), 49–58. https://doi.org/10.1002/zamm.19290090104 (in German).
- Robinson, E.A., 1985. Seismic time-invariant convolutional model. Geophysics 50 (12), 2742–2751. https://doi.org/10.1190/1.1441894.
- Ronneberger, O., Fischer, P., Brox, T., 2015. U-net: convolutional networks for biomedical image segmentation. In: Medical Image Computing and Computer-Assisted Intervention, pp. 234–241. https://doi.org/10.1007/978-3-319-24574-4_28.
- Sams, M.S., Andrea, M., 2001. The effect of clay distribution on the elastic properties of sandstones. Geophys. Prospect. 49 (1), 128–150. https://doi.org/10.1046/j.1365-2478.2001.00230.x.
- Sang, K.H., Yin, X.Y., Zhang, F.C., 2021. Machine learning seismic reservoir prediction method based on virtual sample generation. Pet. Sci. 18 (6), 1662–1674. https://doi.org/10.1016/j.petsci.2021.09.034.
- Simonyan, K., Zisserman, A., 2015. Very deep convolutional networks for large-scale image recognition. In: International Conference on Learning Representations (ICLR). https://arxiv.org/abs/1409.1556.

- Smith, G.C., Gidlow, P.M., 1987. Weighted stacking for rock property estimation and detection of gas. Geophys. Prospect. 35 (9), 993–1014. https://doi.org/10.1111/j.1365-2478.1987.tb00856.x.
- Sun, Q.H., Zong, Z.Y., Li, X., 2024a. Probabilistic seismic inversion based on physics-guided deep mixture density network. Pet. Sci. 21 (3), 1611–1631. https://doi.org/10.1016/j.petsci.2023.12.015.
- Sun, S., Zhao, L., Chen, H., et al., 2023. Prestack seismic inversion for elastic parameters using model-data-driven generative adversarial networks. Geophysics 88 (2), M87–M103. https://doi.org/10.1190/geo2022-0314.1.
- Sun, Y.H., Dong, H.L., Chen, G., et al., 2024b. Intelligent seismic AVO inversion method for brittleness index of shale oil reservoirs. Pet. Sci. 22 (2), 627–640. https://doi.org/10.1016/j.petsci.2024.09.024.
- Voigt, W., 1966. Lehrbuch der Kristallphysik, Forgotten Books , Wiesbaden.
- Wang, P., Cui, Y.A., Du, X., 2022a. Improved prior construction for probabilistic seismic prediction. Geosci. Rem. Sens. Lett. IEEE 19, 1–5. https://doi.org/ 10.1109/LGRS.2022.3175966.
- Wang, P., Cui, Y.A., Zhou, L., et al., 2024. Multi-task learning for seismic elastic parameter inversion with the lateral constraint of angle-gather difference. Pet. Sci. 21 (6), 4001–4009. https://doi.org/10.1016/j.petsci.2024.06.010.
- Wang, Y.Q., Wang, Q., Lu, W.K., et al., 2022b. Seismic impedance inversion based on cycle-consistent generative adversarial network. Pet. Sci. 19 (1), 147–161. https://doi.org/10.1016/j.petsci.2021.09.038.
- Woo, S., Park, J., Lee, J.Y., et al., 2018. CBAM: convolutional block attention module. In: Proceedings of the European Conference on Computer Vision. ECCV), pp. 3–19. https://doi.org/10.1007/978-3-030-01234-2_1.
- Wood, A.B., 1955. A Textbook of Sound, third ed. oriental longmans, Mumbai.
- Xu, S., White, R.E., 1995. A new velocity model for clay-sand mixtures. Geophys. Prospect. 43 (1), 91–118. https://doi.org/10.1111/j.1365-2478.1995. tb00126.x.
- Zhang, K., Lin, N.T., Yang, J.Q., et al., 2022a. Predicting gas-bearing distribution using DNN based on multi-component seismic data: quality evaluation using structural and fracture factors. Pet. Sci. 19 (4), 1566–1581. https://doi.org/10.1016/j.petsci.2022.02.008.
- Zhang, S.B., Si, H.J., Wu, X.M., et al., 2022b. A comparison of deep learning methods for seismic impedance inversion. Pet. Sci. 19 (3), 1019–1030. https://doi.org/10.1016/j.petsci.2022.01.013.
- Zhao, D.F., Yang, N.X., Xiong, J.L., et al., 2023. Model-constrained and data-driven double-supervision acoustic impedance inversion. Pet. Sci. 20 (5), 2809–2821. https://doi.org/10.1016/j.petsci.2023.03.019.
- Zhao, L., Geng, J., Cheng, J., et al., 2014. Probabilistic lithofacies prediction from prestack seismic data in a heterogeneous carbonate reservoir. Geophysics 79 (5), M25–M34. https://doi.org/10.1190/geo2013-0406.1.
- Zheng, Q., Wei, C., Yan, X., et al., 2023. Seismic elastic parameter inversion via a FCRN and GRU hybrid network with multi-task learning. Appl. Sci. 13 (18), 10519. https://doi.org/10.3390/app131810519.
- Zhu, G., Chen, X., Li, J., et al., 2022. Data-Driven seismic impedance inversion based on multi-scale strategy. Remote Sens. 14 (23), 6056. https://doi.org/10.3390/ rs14236056.